

## BIOPHYSICS

# Magnetism and photo dual-controlled supramolecular assembly for suppression of tumor invasion and metastasis

Qilin Yu<sup>1,2</sup>, Ying-Ming Zhang<sup>1</sup>, Yao-Hua Liu<sup>1</sup>, Xun Xu<sup>1</sup>, Yu Liu<sup>1,3\*</sup>

Supramolecular nanoassemblies that respond to multiple stimuli exhibit high therapeutic efficacy against malignant tumors. We report a new type of supramolecular nanofiber that integrates targeting peptide-coated magnetic nanoparticles with  $\beta$ -cyclodextrin-bearing polysaccharides in a complex held together by multivalent interactions. The nanofibers not only exhibited reversible photo-triggered association and disassociation depending on irradiation wavelength but also underwent magnetic field-controlled directional aggregation, even in the rather weak geomagnetic field. The nanofibers markedly suppressed invasion by and metastasis of cancer cells both *in vitro* and *in vivo*. Furthermore, compared with control mice, tumor-burdened mice treated with the nanofibers showed a lower rate of mortality from the metastatic spread of tumor cells. Our results suggest that these geomagnetism- and photo-controlled nanofibers may facilitate the rapid development of efficacious anticancer therapies.

## INTRODUCTION

Although there has been considerable advancement in medical therapies for well-confined primary tumors and early-stage cancer, invasive tumors and metastatic disease remain intractable problems (1–3). Distant metastases are estimated to be responsible for up to 90% of cancer-associated mortality, mainly because metastases are usually inoperable and because disseminated cancer cells are resistant to the therapeutic agents currently in clinical use (4, 5). Therefore, the development of new strategies for impeding tumor growth and preventing metastasis even in advanced-stage disease is imperative. However, the fact that the pathogenic mechanisms involved in the invasiveness and metastasis of tumor cells are poorly understood has hindered the development of effective antimetastatic therapies.

Hope for solutions to the above-described problems has been raised by the recent development of biofunctional supramolecular nanoassemblies that show considerable therapeutic potential (6–8). The noncovalent interactions that hold such nanoassemblies together endow them with the ability to respond dynamically and reversibly to various endogenous and exogenous triggers (9, 10). Consequently, considerable effort has been devoted to exploring the use of nanoassemblies, including nanocarriers, nanoparticles, hydrogels, and (poly)rotaxanes, for controlled and targeted (co)delivery of drugs and genes for the treatment of cancer (11–13). Nanoassembly-based therapies that actively defend against tumor growth and migration—rather than simply passively recognizing and tracking metastatic malignant cells in the manner of conventional tumor therapies—are particularly desirable and would undoubtedly expedite the movement of biofunctional nanoassemblies from the laboratory to the clinic.

Herein, we report supramolecular nanofibers capable of undergoing morphological conversion triggered by photo irradiation or a magnetic field. These unique abilities were derived from the com-

position of the nanofibers, which consisted of biocompatible iron oxide magnetic nanoparticles (MNP) coated with a mitochondrion-targeting peptide (MitP) and covalently cross-linked with hyaluronic acid (HA; a polysaccharide) bearing  $\beta$ -cyclodextrin ( $\beta$ -CD) moieties (HACD) (Fig. 1 and fig. S1). Because HA receptors are over-expressed on the surface of cancer cells, the nanofibers (designated MitP-MNP-HACD), which underwent geomagnetism-directed aggregation, could recruit cancer cells to the nanofibrous network, thereby inhibiting the migration of tumor cells both *in vitro* and *in vivo*. This is the first report of biocompatible supramolecular nanoassemblies that respond to the weak geomagnetic field, and our results may facilitate the development of new types of stimuli-responsive biomaterials that can be used to decrease the rate of mortality from metastatic spread of tumor cells.

## RESULTS AND DISCUSSION

### Formation of binary supramolecular nanoassemblies

Iron oxide MNP was synthesized from  $\text{FeCl}_2$ ,  $\text{FeCl}_3$ , and  $\text{NaOH}$  by means of a coprecipitation method (14). Transmission electron microscopy (TEM) images revealed that the MNP were cube-like and had diameters of 10 to 20 nm (fig. S2A). The x-ray powder diffraction (XRD) pattern of the MNP was coincident with that of pristine  $\text{Fe}_3\text{O}_4$  (fig. S2B) (15). Chemically modifiable  $-\text{NH}_2$  groups were added to the surface of the MNP by means of a silanization reaction with aminopropyltriethoxysilane (APTES). The resulting amino-modified MNP (MNP- $\text{NH}_2$ ) were covalently linked, via glutaraldehyde, to a fluorescein isothiocyanate (FITC)-labeled MitP (FITC-ACP-Fx-r-Fx-K-Fx-r-Fx-K) to endow the MNP with the desired mitochondrion-specific targeting ability (Figs. 1 and 2A and fig. S2, C and D) (16). TEM images of the MitP-MNP indicated that, like the MNP, they were cube-like, but they tended to exist as more condensed nanoclusters (Fig. 2B). Magnified TEM images and Fourier transform infrared spectrum confirmed the presence of MitP on the surface of MNP (fig. S2, E and F).

Considering that the MitP-MNP has numerous pendant cyclohexylalanine groups around their cores, we speculated that larger supramolecular nanoassemblies could be generated through hierarchical intermolecular organization. To evaluate this possibility,

<sup>1</sup>College of Chemistry, State Key Laboratory of Elemento-Organic Chemistry, Nankai University, Tianjin 300071, China. <sup>2</sup>Department of Microbiology, College of Life Sciences, Nankai University, Tianjin 300071, China. <sup>3</sup>Collaborative Innovation Center of Chemical Science and Engineering (Tianjin), Tianjin 300072, China.

\*Corresponding author. Email: yuliu@nankai.edu.cn

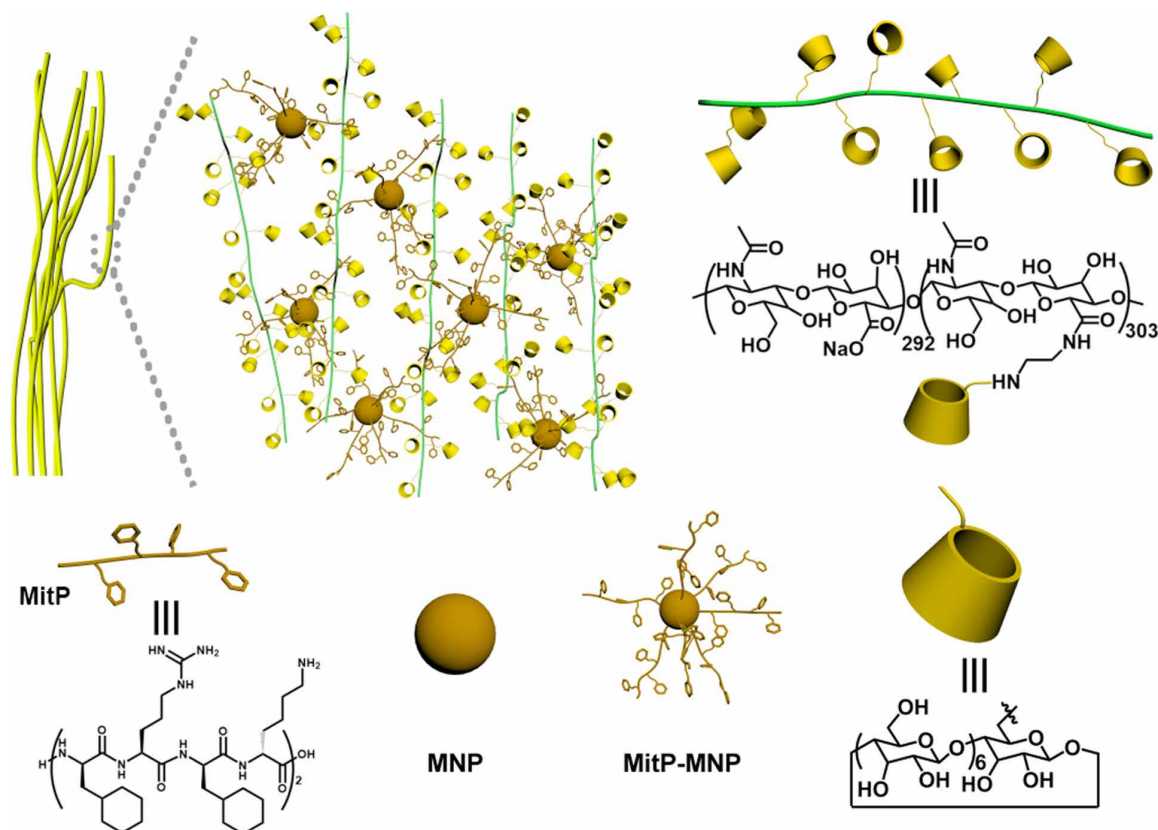


**Fig. 1. Schematic illustration of the formation of MitP-MNPcHACD nanofibers.**

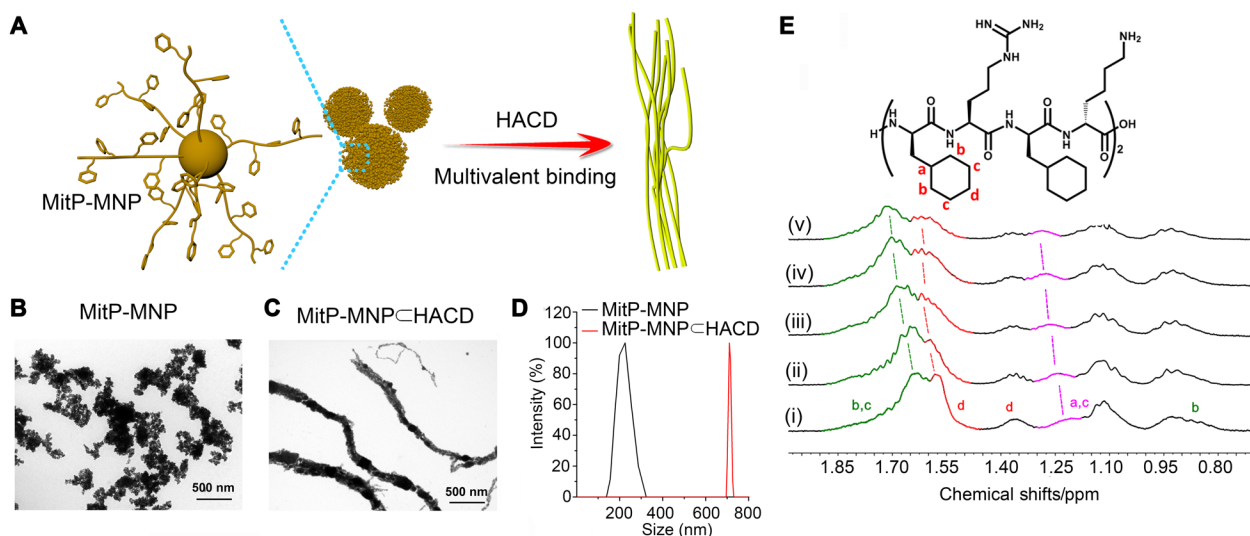


**Fig. 2. Formation and characterization of MitP-MNP and MitP-MNPcHACD nanofibers.** (A) Schematic illustration of formation of MitP-MNPcHACD nanofibers by cross-linking HACD with MitP-MNP. (B and C) TEM images and (D) dynamic light scattering (DLS) data for MitP-MNP and MitP-MNPcHACD nanofibers ([MitP-MNP] = 0.2 mg/ml and [HACD] = 0.2 mg/ml). (E) <sup>1</sup>H nuclear magnetic resonance (NMR) titration of MitP with native β-CD, revealing that the cyclohexyl groups of MitP were included in the β-CD cavity: MitP alone (i) and [MitP]:[β-CD] [1:1, 1:2, 1:3, and 1:4 (ii to v), respectively]. ppm, parts per million.

we selected HACD as a cross-linker because we expected that strong inclusion complexation would occur via multivalent binding between the β-CD cavity and the hydrophobic cyclohexyl groups of MitP (17). TEM images revealed that MitP-MNP and HACD self-assembled via noncovalent interactions to form nanofibers that were

100 to 500 nm in diameter and several micrometers long (Fig. 2C and fig. S3A). DLS analysis demonstrated that the hydrodynamic diameter of these MitP-MNPcHACD nanofibers (710 nm) was remarkably larger than that of the MitP-MNP (205 nm), and the size distribution of the assemblies in the presence of HACD was

narrower than that in the absence of HACD (Fig. 2D).  $^1\text{H}$  NMR spectroscopy revealed that the cyclohexyl protons of MitP ( $\text{H}_{\text{a-d}}$ ) shifted downfield upon addition of native  $\beta$ -CD, indicating that the cyclohexyl groups became encapsulated in the  $\beta$ -CD cavity (Fig. 2E).

To confirm that inclusion complexation played a role in the formation of the MitP-MNP $\subset$ HACD nanofibers, we carried out some control experiments. Nanofiber formation was not observed when MitP-MNP was mixed with natural HA or when MNP was mixed with HACD (fig. S3, B and C). Moreover, the addition of 1-adamantanecarboxylic acid (ADA), which binds strongly to  $\beta$ -CD, drastically attenuated the formation of MitP-MNP $\subset$ HACD nanofibers (fig. S3D). Together, these observations confirm that electrostatic interactions between the positively charged MitP molecules on the MitP-MNP and the negatively charged carboxylic groups on the HA backbone were not sufficient for the formation of MitP-MNP $\subset$ HACD nanofibers and that the multiple noncovalent cross-linking interactions between  $\beta$ -CD and the cyclohexylalanine moieties of the MitP were indispensable for stabilizing the nanofibrous structure.

### Geomagnetism-controlled formation of the supramolecular nanoassemblies

Using FITC-labeled MitP as a fluorescent probe, we monitored the formation of the MitP-MNP $\subset$ HACD nanofibers in real time by means of confocal microscopy. When MitP-MNP and HACD were mixed together, they interacted dynamically to form small (50  $\mu\text{m}$  long) aggregates within 2 min (Fig. 3A). As the incubation time

increased, the aggregates slowly grew larger, first forming short nanofibers (Fig. 3A, 5 min) and eventually self-assembling into stable, higher-order 50- to 100- $\mu\text{m}$ -long nanofibers after 10 min (Fig. 3A and movie S1). We measured the angle ( $\delta$ , in degrees) between the geomagnetic field line and the growth direction and observed no obvious declination between the geomagnetic field line and the growth direction ( $\delta < \pm 5^\circ$ ; table S1). We also found that when the orientation of the microscope relative to the geomagnetic field line was changed, the growth direction changed accordingly (Fig. 3B and movies S2 and S3). Together, these results indicate that the direction of the growth of the nanofibers aligned perfectly with the geomagnetic field.

Furthermore, when we used a field-canceling system to shield the sample from any artificial magnetic fields, the formation of MitP-MNP $\subset$ HACD nanofibers was still observed in the pure geomagnetic field (0.048 mT; Fig. 3C and movie S4). In distinct contrast, directional growth of nanofibers did not occur when the experiment was carried out in a metal-caged room that was largely shielded from the geomagnetic field (0.015 mT; Fig. 3D and movie S5). On the basis of these results, we concluded that MitP-MNP $\subset$ HACD nanofibers formed only when the weak geomagnetic field was present and that, like a compass needle, the direction of nanofiber growth was controlled by the geomagnetic field. We suggest that the high sensitivity to the geomagnetic field orientation was due mainly to multivalent cross-linking of numerous MNP with polymeric HACD, resulting in formation of supramolecular nanofibers enriched in discrete, small MNP along their lengths.

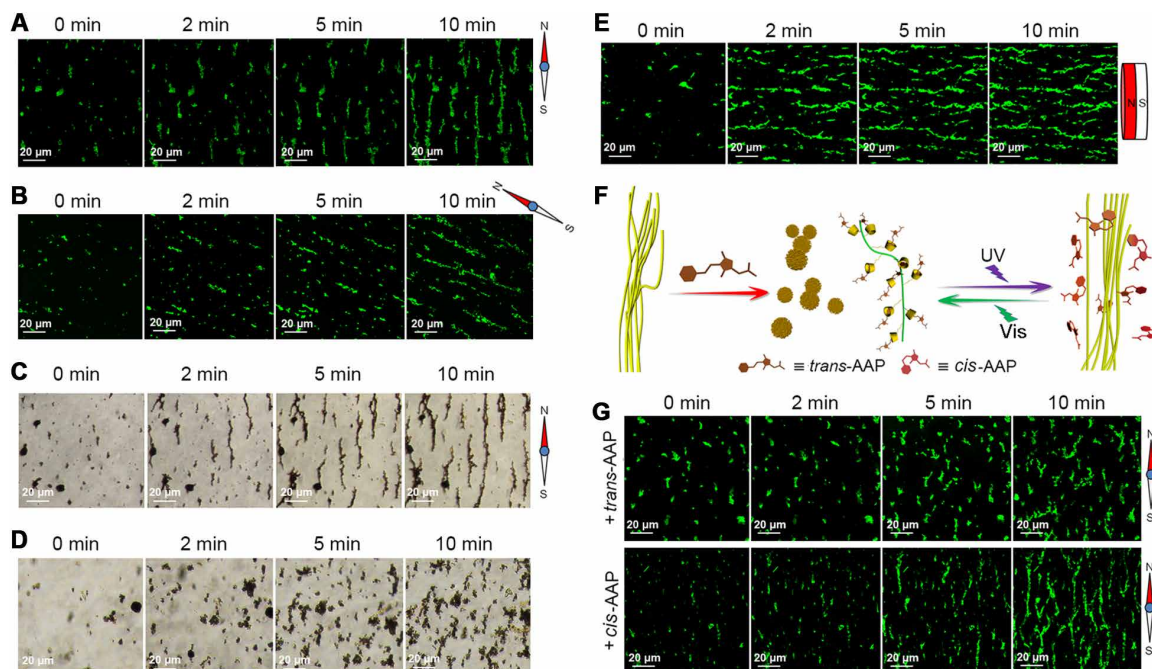


**Fig. 3. Magnetism- and photo-controlled assembly of MitP-MNP $\subset$ HACD nanofibers.** (A and B) Confocal microscopy images of the growth of MitP-MNP $\subset$ HACD nanofibers along the direction of the geomagnetic field (0.050 mT). (C and D) Light microscopy images of the growth of MitP-MNP $\subset$ HACD nanofibers in a pure geomagnetic field (0.048 mT; C) and in a metal-caged room with a decreased geomagnetic field (0.015 mT; D). (E) Confocal microscopy images of the growth of MitP-MNP $\subset$ HACD nanofibers along the direction of an artificial magnetic field (0.308 mT). (F) Schematic illustration of photoresponsive assembly and disassembly of MitP-MNP $\subset$ HACD nanofibers in the presence of an arylazopyrazole (AAP) carboxylate ([MitP-MNP] = 0.2 mg/ml, [HACD] = 0.2 mg/ml, and [AAP] = 0.2 mg/ml). Vis, visible. (G) Confocal microscopy images showing the temporal dependence of nanofiber growth in the presence of *trans*-AAP and *cis*-AAP carboxylates [generated by ultraviolet (UV) irradiation at 365 nm].

Owing to their iron oxide cores, the MitP-MNP $\subset$ HACD nanofibers could also form under the control of an artificial magnetic field. Specifically, when MitP-MNP and HACD were exposed to the field of a strong magnet, nanofibers instantly formed and quickly grew along the direction of the magnetic field. Stable fibers were observed after only 2 min (Fig. 3E, table S1, and movies S6 and S7). Moreover, increasing the magnetic field strength accelerated the growth of the nanofibers (table S1).

### Photoresponsiveness of the supramolecular nanoassemblies

The photoresponsiveness of the nanofibers was tested with a competitive guest molecule, an AAP carboxylate. AAPs are photoactive molecules that reversibly form inclusion complexes with  $\beta$ -CD upon photoisomerization from the *cis* isomer to the *trans* isomer (18). The addition of *trans*-AAP carboxylate to the MitP-MNP $\subset$ HACD nanofibers seriously disrupted the organization of the fibers and resulted in the formation of disordered nanoaggregates (Fig. 3, F and G, +*trans*-AAP). We attributed this phenomenon to the *trans*-AAP carboxylate competitively inhibiting formation of an inclusion complex between HACD and MitP-MNP (Fig. 3F). When the disordered aggregates were irradiated at 365 nm (UV) to convert the *trans*-AAP carboxylate to *cis*-AAP carboxylate, the regular nanofibers reformed and exhibited magnetism-responsive behavior because *cis*-AAP carboxylate could not fit in the  $\beta$ -CD cavity (Fig. 3G). We also investigated the reversibility of this photocontrolled morphological conversion by alternating UV and visible light irradiation. A ternary system comprising HACD, MitP-MNP, and *trans*-AAP carboxylate formed randomly distributed nanoclusters and nanoparticles. Irradiation at 365 nm for 10 min resulted in the gradual conversion of the disordered nanoclusters into regular nanofibers that grew along the direction of the geomagnetic field. Subsequent irradiation at 520 nm disassembled the nanofibers, but they could be reassembled by irradiation at 365 nm (fig. S3E).

### Recruitment of mitochondria with the supramolecular nanoassemblies

The presence of the targeting peptides on the surface of the iron oxide nanoparticles allowed us to investigate the specific interaction of the MitP-MNP $\subset$ HACD nanofibers with mitochondria because of the intrinsic high negative membrane potential of this organelle (19). Mitochondria were isolated from human lung cancer cells (A549), stained with 4',6-diamidino-2-phenylindole (DAPI) and then coincubated with MitP-MNP and HACD. Initially, the DAPI-labeled organelles were dispersed randomly among MitP-MNP. As the MitP-MNP $\subset$ HACD nanofibers formed and grew along the direction of the geomagnetic field, the mitochondria gradually aggregated around nanofibers, which grew at a rate of 0.271  $\mu\text{m/s}$  (Fig. 4, A and B, 2 to 5 min). Eventually, stable fiber-like structures formed and were observed to be colocalized with the mitochondria (Fig. 4, A and B, 10 min). Moreover, we found that the addition of ADA inhibited the formation of mitochondrial fibers (fig. S4A), again confirming that the assembly of these organelles among the MitP-MNP $\subset$ HACD nanofibers was dependent on the supramolecular interaction between  $\beta$ -CD and MitP. In addition, we found that under the influence of an artificial magnetic field, the mitochondria rapidly fused with the MitP-MNP $\subset$ HACD nanofibers along the orientation of external magnetic field at an assembly rate of 0.305  $\mu\text{m/s}$  (fig. S4B). These observations demonstrate that the supramolecular assembly maintained its nanofibrous morphology

and its mitochondrion-specific targeting ability during the assembly process.

### Intracellular damage to mitochondria by the supramolecular nanoassemblies

Because the MitP-MNP $\subset$ HACD nanofibers could recruit isolated mitochondria, we hypothesized that the nanofibers might also interact with intracellular mitochondria and affect their function. Consistent with this hypothesis, confocal microscopy revealed that the MitP-MNP $\subset$ HACD nanofibers, similar to MitP-MNP, were localized mainly at the mitochondria in A549 tumor cells (Fig. 4C), suggesting that the nanofibers could enter the tumor cells and bind the mitochondria. Especially noteworthy is the fact that the MitP-MNP $\subset$ HACD nanofibers maintained their morphology inside the tumor cells (Fig. 4C and fig. S5), indicating the high stability of these supramolecular nanoassemblies in the intracellular environment. For comparison, the actin-targeting peptide ABP140 was used as a negative control (20). ABP140 was grafted onto the surface of MNP to obtain ABP-MNP, which were found to lack mitochondrion-targeting ability. ABP-MNP was not specifically located at the mitochondria (fig. S6), indicating that MitP was necessary for specific mitochondrial targeting (16). Moreover, although control cells and MitP-MNP-treated cells showed normal network-like mitochondrial morphology, cells treated with the MitP-MNP $\subset$ HACD nanofibers exhibited dotted mitochondrial morphology, indicative of mitochondrial damage (Fig. 4C and fig. S5). Western blotting of cytochrome C and cleaved caspase-3 (activated caspase-3) and an intracellular ATP assay indicated that, compared with MitP-MNP, MitP-MNP $\subset$ HACD nanofibers caused higher levels of cytochrome C release from the mitochondria to the cytoplasm and greater activation of caspase-3 (Fig. 4, D to F) and that the presence of nanofibers caused a decrease of cellular ATP production after 24 hours (Fig. 4G).

Mitochondrial damage is an important inducer of cell cycle arrest and apoptosis, which in turn result in a decrease in cell viability (21, 22). A cell viability assay showed that A549 tumor cells treated with MitP-MNP $\subset$ HACD nanofibers showed remarkably decreased cell viability relative to cells treated with MitP-MNP alone (48.2% versus 99.1% at an MitP-MNP concentration of 80 mg/liter) (Fig. 4H and fig. S7A). In addition, flow cytometry of the cells stained with propidium iodide (PI) revealed that the MitP-MNP $\subset$ HACD nanofibers caused a decrease in the percentages of both G2- and S-phase cells and a remarkable increase in the percentage of apoptotic cells (to 25.11%), whereas MitP-MNP alone had no obvious impact on cell cycle progression (Fig. 4I). In addition, treatment with HACD alone had no effect on cell viability (fig. S7B), confirming the role of the supramolecular nanoassemblies in the decrease in cell viability. We also carried out PI staining experiments to determine whether mitochondrial damage was the immediate cause of cell death in our system (fig. S7, C and D). After incubation with MitP-MNP $\subset$ HACD nanofibers for 24 hours, the percentage of dead cells was quite low (<9%), but after 48 hours, the percentage increased remarkably (to 35%). The low percentage of dead cells after 24 hours suggests that cell death did not contribute to mitochondrial damage. On the basis of the fact that severe mitochondrial damage occurred within 24 hours (Fig. 4, C to E), we can deduce that the MitP-MNP $\subset$ HACD nanofibers directly damaged the mitochondria and then induced a decrease in cell viability related to apoptosis and cell cycle arrest (Fig. 4, F and I), even though it has been shown that some fibrillar

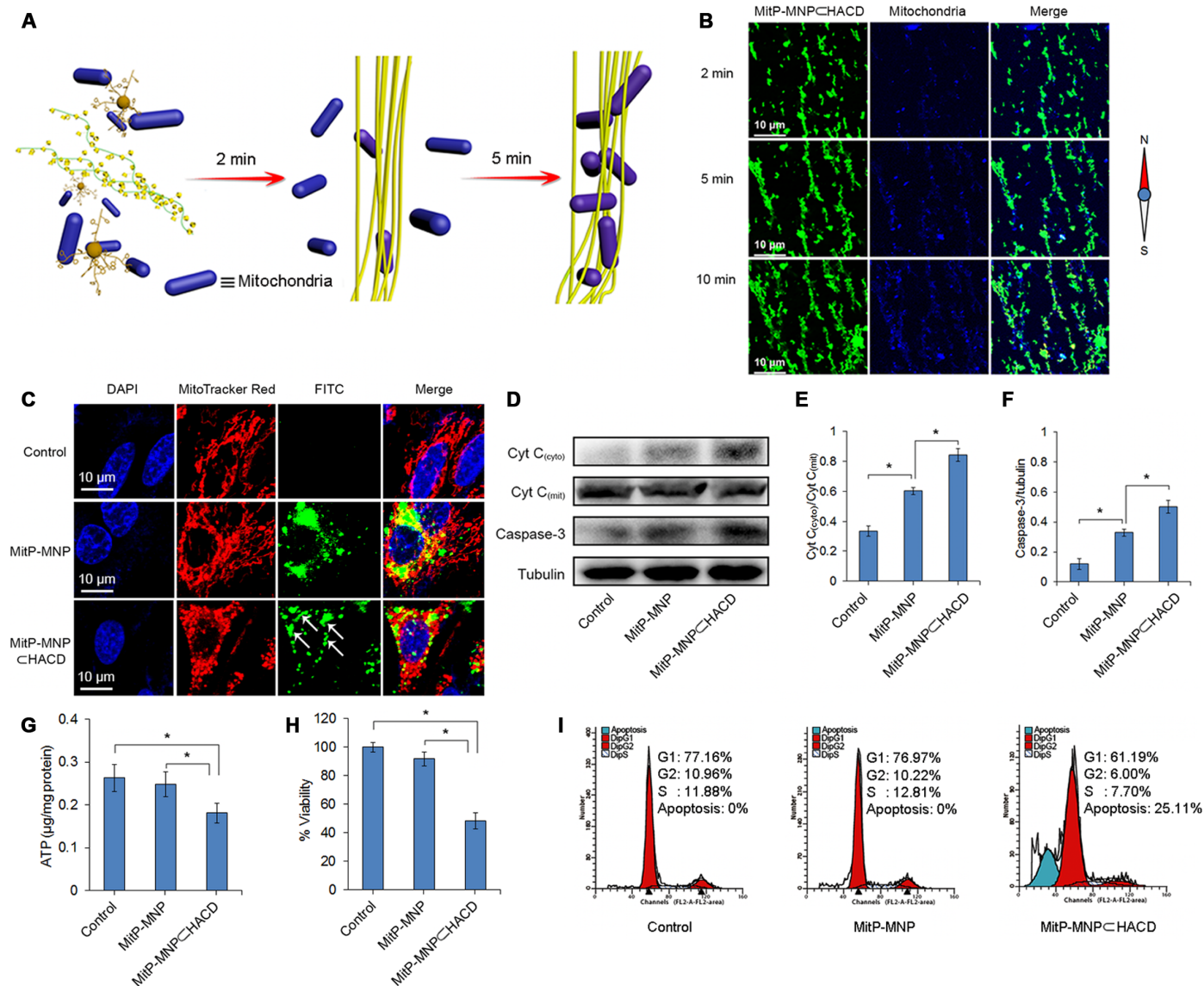


**Fig. 4. Interaction of MitP-MNP $\subset$ HACD nanofibers with mitochondria and disruption of mitochondrial function in A549 tumor cells by the nanofibers.** (A) Schematic illustration of aggregation of mitochondria around MitP-MNP $\subset$ HACD nanofibers along the direction of the geomagnetic field (0.050 mT). (B) Confocal microscopy images of DAPI-labeled mitochondria incubated with MitP-MNP and HACD for 2, 5, and 10 min ([MitP-MNP] = 0.2 mg/ml and [HACD] = 0.2 mg/ml). (C) Confocal microscopy images of cells treated with MitP-MNP alone or with MitP-MNP $\subset$ HACD nanofibers (white arrows indicate intracellular nanofibers). (D) Images of Western blots of cytoplasmic and mitochondrial cytochrome C [Cyt C<sub>(cyto)</sub> and Cyt C<sub>(mit)</sub>], cleaved caspase-3 (an apoptosis-inducing factor), and tubulin. (E) Ratio of Cyt C<sub>(cyto)</sub> to Cyt C<sub>(mit)</sub>. (F) Ratio of cleaved caspase-3 to tubulin. (G) Decrease of intracellular adenosine 5'-triphosphate (ATP) production caused by MitP-MNP $\subset$ HACD nanofibers. (H) Decrease in cell viability caused by MitP-MNP $\subset$ HACD nanofibers. (I) Cell cycle arrest and apoptosis caused by MitP-MNP $\subset$ HACD nanofibers. Asterisks in E to H indicate statistically significant differences between groups ( $P < 0.05$ ).

assemblies within cells are capable of inducing severe cell death independent of aggregation of mitochondria (23, 24).

**Suppression of tumor invasion and metastasis by the supramolecular nanoassemblies**

Further investigation revealed that the MitP-MNP $\subset$ HACD nanofibers strongly inhibited tumor cell invasion and metastasis. Specifically, in a Matrigel invasion model, the intercellular formation of MitP-MNP $\subset$ HACD nanofibers (Fig. 5, A and B) resulted in aggregation of red fluorescent protein (RFP)-tagged tumor cells (A549-Luc2-tdT-2) and severe attenuation of cell invasion into the

Matrigel (Fig. 5, B to D). In contrast, MitP-MNP was uniformly distributed in the Matrigel in a nanoparticulate state and had little impact on cell invasion (Fig. 5, B to D). No nanofibrous structure was found inside the invading cells after treatment with the MitP-MNP $\subset$ HACD nanofibers (fig. S8), indicating that the Matrigel as a confined environment may have hindered internalization of the nanofibers and that the extracellular nanofibers may have served as a barrier to cell migration. Moreover, whereas control cells and MitP-MNP-treated cells recovered their growth activity (as indicated by red fluorescence) and migrated onto the scraped gaps, the MitP-MNP $\subset$ HACD-treated cells failed to grow or migrate (Fig. 5E).

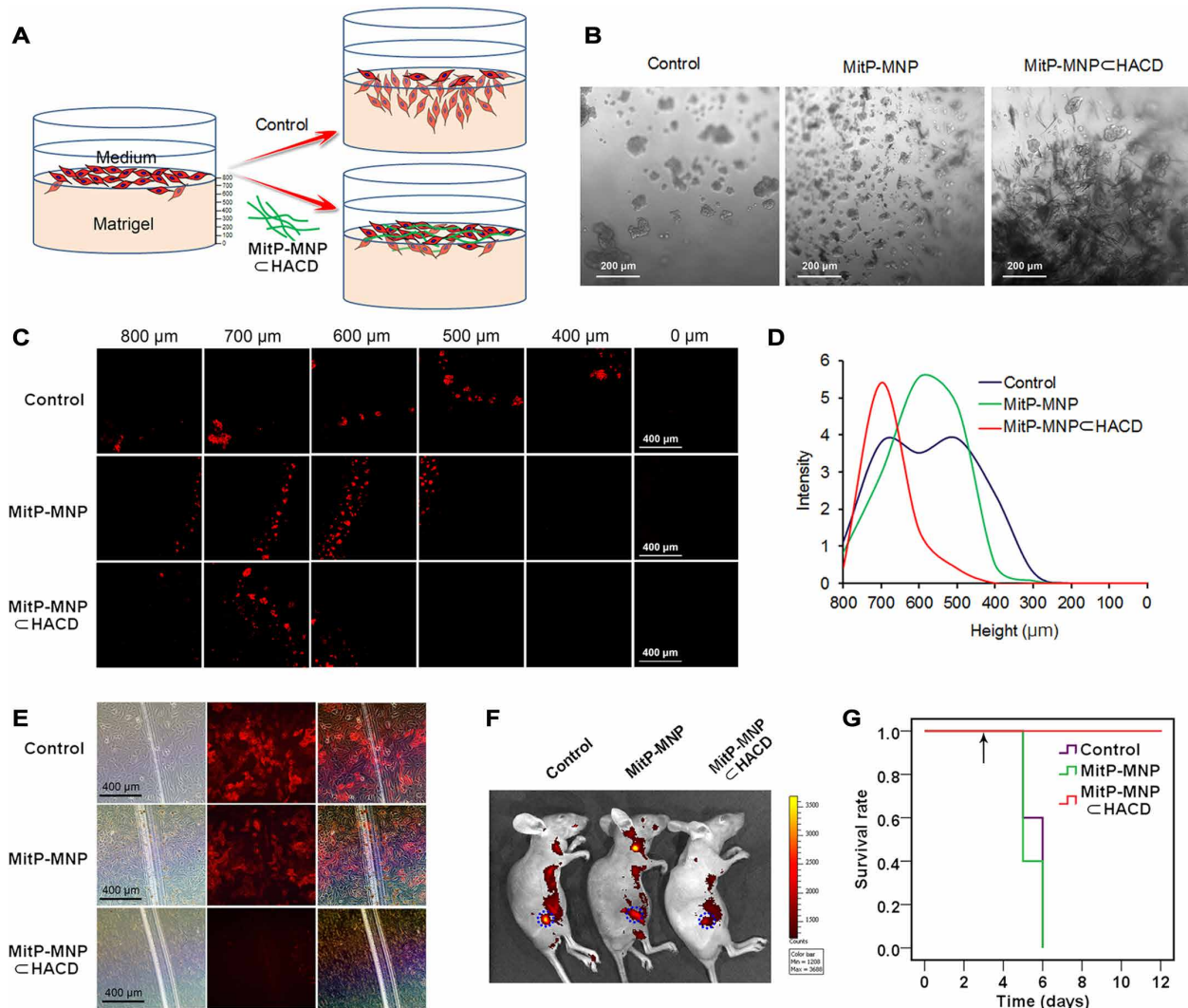


**Fig. 5. Suppression of tumor cell invasion and metastasis by MitP-MNP $\subset$ HACD nanofibers both in vitro and in vivo.** (A) Schematic illustration of inhibition of tumor cell invasion into Matrigel by MitP-MNP $\subset$ HACD nanofibers. (B) Light microscopy images of the interaction between RFP-tagged A549 lung tumor cells and MitP-MNP $\subset$ HACD nanofibers during invasion into the Matrigel. (C) Confocal microscopy images of the invading tumor cells at various heights in the Matrigel. (D) Quantification of the fluorescence intensity of the tumor cells at various heights in the Matrigel. (E) Images of migration of the A549 cells to the scraped gaps. (F) In vivo inhibition of A549 cell metastasis by MitP-MNP $\subset$ HACD nanofibers (dotted blue circles indicate tumor cell injection sites). (G) Survival curve for mice with A549 metastases; the black arrow indicates the time at which MitP-MNP or MitP-MNP $\subset$ HACD nanofibers were injected into the mice.

Consistent with the above-described results, experiments with a murine in vivo tumor metastasis model showed that the MitP-MNP $\subset$ HACD nanofibers strongly suppressed migration of RFP-tagged tumor cells, restricting the cells to locations near the site at which they had been injected. In contrast, injection of MitP-MNP alone failed to inhibit tumor metastasis; tumor cells migrated all the way from the injection site to the neck (Fig. 5F). More strikingly, all of the tumor-burdened mice survived after treatment with the MitP-MNP $\subset$ HACD nanofibers, whereas control mice and MitP-MNP-treated mice died 6 days after injection of the tumor cells (Fig. 5G). Flow cytometry revealed that the nanofibers bound much more strongly to RFP-tagged tumor cells than to untagged 293T normal cells (fig. S9A), indicating that the HA-containing nanofibers actively targeted the tumor cells (17, 25, 26). Furthermore, histopathological analysis revealed that the nanofibers had no impact on the reticulo-

endothelial system (RES) organs, including the liver, spleen, and kidney (fig. S9B), suggesting that the nanofibers had good biocompatibility. Together, these results suggest that the biocompatible MitP-MNP $\subset$ HACD nanofibers could efficiently suppress tumor cell invasion and metastasis.

## CONCLUSION

In conclusion, we used a molecular assembly process to construct binary nanofibers composed of MNP modified with a targeting peptide (MitP) and a  $\beta$ -CD-grafted polysaccharide (HACD). The assembly process could be regulated both by a (geo)magnetic field and by light. Furthermore, the resulting biocompatible MitP-MNP $\subset$ HACD nanofibers could induce mitochondrial dysfunction and intercellular aggregation, ultimately leading to the specific

suppression of tumor cell invasion and metastasis *in vivo*. On the basis of the results reported herein, we suggest that the MitP-MNP $\square$ HACD nanofibers could serve as a convenient tool not only for deepening our understanding of dynamic, stimuli-responsive biological events but also for facilitating the development of intelligently designed bioinspired materials for tumor therapy.

## MATERIALS AND METHODS

### Chemicals and instruments

APTES and glutaraldehyde were purchased from Sigma-Aldrich. All other reagents were purchased from Aladdin. HACD was synthesized by means of an amide condensation reaction between HA sodium salt and mono-6-deoxyl-6-ethylenediamino- $\beta$ -CD, according to a previously reported procedure (17). NMR spectra were recorded on a Bruker AV400 instrument in D<sub>2</sub>O. DLS analysis was performed on a laser light scattering spectrometer (BI-200SM) equipped with a digital correlator (TurboCorr) at 636 nm at a scattering angle of 90°.

### Synthesis of FITC-labeled MitP (16)

FITC-labeled MitP (FITC-ACP-Fx-r-Fx-K-Fx-r-Fx-K,  $M_w = 1701$ ) was synthesized by means of the solid phase method by Beijing Protein Innovation Ltd. The peptide was characterized by high-performance liquid chromatography (LC3000, Constant Innovation; fig. S2) and mass spectrometry (LC-MS2010, Shimadzu; fig. S2).

### Synthesis of MNP

The MNP used in this study were prepared by the coprecipitation method. Briefly, 100 ml of a 0.3 M solution of FeCl<sub>2</sub> in distilled water was mixed with 100 ml of a 0.6 M solution of FeCl<sub>3</sub> in distilled water. Then, 0.3 M NaOH (100 ml) was slowly added to the mixture. The resulting black solution was heated to precipitate the MNP. After the MNP were washed with distilled water until the pH of the wash solution was 7.0, they were dried at room temperature before further use. The morphology of the obtained MNP was characterized by means of TEM (Tecnai G<sup>2</sup> F-20, FEI). The crystal structure and composition of the MNP were characterized by XRD analysis (D/max-2500).

The magnetic field strengths in the environment of pure geomagnetic field or artificial magnetic field and in a metal-caged room were measured with a standard Gauss meter (Beiyi-601, Pafei). Supramolecular nanoassemblies and cells were observed with a confocal microscope (FV1000, Olympus), a light microscope (CKX53, Olympus), or a fluorescence microscope (DM3000, Leica).

### Synthesis and characterization of MitP-MNP, ABP-MNP, and MitP-MNP $\square$ HACD nanofibers

For preparation of MitP-MNP, MNP (40 mg) were suspended in 40 ml of ethanol, and then, 2 ml of APTES was added. The mixture was magnetically stirred at 80°C for 2 hours and then centrifuged, and the pellet was washed thrice with ethanol and twice with distilled water to afford MNP-NH<sub>2</sub>. The MNP-NH<sub>2</sub> was suspended in 30 ml of 8% glutaraldehyde [prepared in phosphate-buffered saline (PBS; pH 7.4)]. The suspension was gently shaken for 6 hours at room temperature and then centrifuged to pellet MNP-NH<sub>2</sub>-glutaraldehyde. The pellet was washed thrice with PBS and then suspended in 20 ml of the same buffer. MitP (400  $\mu$ l, 1 mM in PBS) was added to the suspension, which was shaken at 120 rpm at 4°C for 24 hours. The resulting solid was separated by centrifugation, and the

pellet was washed twice with distilled water and lyophilized in a freezing vacuum dryer to afford MitP-MNP.

ABP-MNP was synthesized as a negative control as described above, except that FITC-tagged ABP140 (FITC-ACP-M-G-V-A-D-L-I-K-K-F-E-S-I-S-K-E-E-C) was used to react with MNP-NH<sub>2</sub>-glutaraldehyde (20). The MitP-MNP $\square$ HACD nanofibers were formed by mixing the MitP-MNP and HACD (0.2 mg/ml, respectively), followed by sonication for 5 min. The formation of MitP-MNP and the MitP-MNP $\square$ HACD nanofibers was monitored by TEM, confocal microscopy, and DLS analysis.

### Confocal microscopy observation of the supramolecular nanoassemblies

In a typical procedure, MitP-MNP and HACD were mixed in distilled water ([MitP-MNP] = 0.2 mg/ml, [HACD] = 0.2 mg/ml), and the mixture was sonicated for 5 min (AS3120, Auto Science), placed in a culture dish, and immediately observed under a confocal or light microscope in the laboratory. In addition, to elucidate the effect of the geomagnetic field, we also observed nanofiber assembly in a room equipped with a field-canceling system (SC22, Spicer Consulting) that blocked artificial magnetic fields or in a metal-caged TEM room to block the geomagnetic field. To explore the relationship between the magnetic field strength and the growth rate of the nanofibers, we plotted nanofiber length against time at various magnetic field strengths and calculated the growth rates of the nanofibers.

### Isolation and staining of mitochondria

Mitochondria were isolated from human lung tumor cells (A549), which were purchased from the Cell Resource Center, China Academy of Medical Science, and cultured in F12 medium supplemented with 10% fetal bovine serum (FBS; Hyclone) in a CO<sub>2</sub> incubator at 37°C for 24 hours. The cultured cells were dispersed in 0.25% trypsin-EDTA solution (Dingguo, China) and harvested by centrifugation. The obtained cells were suspended in mitochondrial buffer [sucrose, 210 mM; mannitol, 70 mM; EDTA, 1 mM; EGTA, 1 mM; MgCl<sub>2</sub>, 1.5 mM; HEPES, 10 mM (pH 7.2)] to 5  $\times$  10<sup>7</sup> cells/ml, and 1 ml of the suspension was homogenized with a Dounce homogenizer (20 to 50 strokes). Cell lysates were centrifuged at 1000g and 4°C to remove the nuclei and intact cells. The supernatant was further centrifuged at 10,000g to obtain the mitochondria. The mitochondria were resuspended in 500  $\mu$ l of mitochondrial buffer and stained with 5  $\mu$ l of DAPI (1 mg/ml; Sigma-Aldrich) at 37°C for 30 min. The stained mitochondria were centrifuged at 10,000g for 5 min, and the pellet was washed twice with mitochondrial buffer and resuspended in 500  $\mu$ l of the same buffer (0.5 mg proteins/ml).

### Observation of intracellular supramolecular nanoassemblies by confocal microscopy

The A549 cells were incubated with MitP-MNP (80 mg/liter) or with MitP-MNP (80 mg/liter) plus HACD (80 mg/liter) (MitP-MNP $\square$ HACD) for 24 hours. The cells were then washed with PBS, stained with MitoTracker Red (100 nM; Sigma-Aldrich) at 37°C for 40 min, and fixed with 4% formaldehyde. The fixed cells were stained with DAPI (5 mg/liter) or Hoechst 33342 (5 mg/liter) and observed by confocal microscopy.

### Western blotting

The A549 cells were treated with MitP-MNP (80 mg/liter) or with MitP-MNP (80 mg/liter) plus HACD (80 mg/liter) (MitP-MNP $\square$ HACD)

for 24 hours to extract the mitochondria or the total intracellular proteins. For detection of both cytoplasmic and mitochondrial cytochrome C, the cells were homogenized with a Dounce homogenizer (20 to 50 strokes). The cell lysate was centrifuged at 1000g and 4°C to remove nuclei and intact cells. The resulting suspension was then centrifuged at 10,000g to obtain the cytoplasm (supernatant) and the mitochondria (pellet), respectively. The levels of cytoplasmic and mitochondrial cytochrome C were detected with cytochrome C monoclonal antibody (Abcam).

For determination of the level of cleaved caspase-3, the treated cells were lysed with radioimmunoprecipitation assay (RIPA) buffer, and cleaved caspase-3 was detected with the corresponding monoclonal antibody (Abcam). A control protein, tubulin, was detected with tubulin monoclonal antibody (Abcam). The bands in the blots were quantified by means of ImageJ software (version 2).

### ATP assay

The levels of intracellular ATP in the treated A549 cells were determined by means of the ATP Assay Kit (Beyotime) in accordance with the manufacturer's instructions. A fluorescence microplate reader (Enspire, PerkinElmer) was used to determine luminescence density, which reflects intracellular ATP levels.

### Cell viability assay

The A549 cells were treated with MitP-MNP, MitP-MNP $\subset$ HACD, or HACD at concentrations ranging from 0 to 80 mg/liter. The viability of the treated cells was then determined with the CCK-8 Assay Kit (Dojindo). Cell death was assessed by means of PI staining after 24 and 48 hours.

### Cell cycle analysis

The treated A549 cells were washed twice with PBS and fixed overnight with 95% ethanol. The fixed cells were suspended in 50 mM citrate buffer (pH 7.4), treated with ribonuclease (0.5 mg/ml; Sigma-Aldrich) at 37°C for 1 hour, and then stained with PI (20 mg/liter) for flow cytometry analysis.

### In vitro tumor cell invasion and migration assay

The RFP-tagged A549 cell line A549-Luc2-tdT-2 (Cell Resource Center, China Academy of Medical Science) was cultured in McCoy's 5A medium supplemented with 10% FBS (Hyclone) in a CO<sub>2</sub> incubator at 37°C for 48 hours. The cells were then suspended in FBS-free McCoy's 5A medium at  $5 \times 10^5$  cells/ml. Matrigel (Corning) was diluted in coating buffer [0.01 M tris, 0.7% NaCl (pH 8.0)] to a final concentration of 300  $\mu$ g/ml and then placed in 24-well invasion chambers (immersed in McCoy's 5A medium supplemented with 10% FBS) to a gel height of 800  $\mu$ m. The chambers were incubated at 37°C for 2 hours for gelation. Cell suspension (500  $\mu$ l) was added to the chambers, and then MitP-MNP (80 mg/liter) or MitP-MNP (80 mg/liter) plus HACD (80 mg/liter) (MitP-MNP $\subset$ HACD) was added. The cells were cultured for 12 hours, and then cells that had invaded the Matrigel were observed by confocal microscopy. The fluorescence intensity of the cells at different heights in the Matrigel was quantified by means of ImageJ software. For detection of intracellular formation of MitP-MNP $\subset$ HACD nanofibers, the Matrigel was treated with trypsin (2.5%; Gibco) and washed with PBS to release the invading cells. The obtained cells were then washed thrice with PBS and observed by fluorescence microscopy.

In vitro migration of the A549-Luc2-tdT-2 cells was assessed in six-well microplates as follows. Partial cells that adhered to the well bottom surface were scraped off with a tweezer to form a gap, and the remaining adhered cells were treated with MitP-MNP (80 mg/liter) or MitP-MNP (80 mg/liter) plus HACD (80 mg/liter) (MitP-MNP $\subset$ HACD) for 12 hours. Then, cell migration into the gaps was observed.

### In vivo model of tumor metastasis

In vivo tumor metastasis was evaluated in A549-Luc2-tdT-2-bearing nude mice (Huaafukang) as follows. Fifteen 4-week-old female BALB/c nude mice were pretreated with cyclophosphamide (200 mg/kg) for 2 days. Then, the mice were inoculated subcutaneously with 200  $\mu$ l of an A549-Luc2-tdT-2 cell suspension ( $1 \times 10^8$  cells/ml) and divided into three groups (five mice per group). Three days after inoculation, MitP-MNP (80 mg/kg) or MitP-MNP $\subset$ HACD nanofibers [MitP-MNP (80 mg/kg) plus HACD (80 mg/kg)] were intravenously injected into the mice; a control group received only saline. Distribution of the A549-Luc2-tdT-2 cells in the mice was observed 2 days after injection. The survival rate of the mice was recorded. All animal experiments were approved by the Animal Care and Use Committee at Nankai University.

### Targeting of MitP-MNP $\subset$ HACD nanofibers to tumor cells

To investigate the targeting of MitP-MNP $\subset$ HACD nanofibers to tumor cells, we mixed A549-Luc2-tdT-2 tumor cells with human embryonic kidney 293T cells (normal cells) at a 1:4 ratio and cocultured the cells in Dulbecco's modified Eagle's medium supplemented with 10% FBS for 24 hours. The mixed cells were then treated with MitP-MNP $\subset$ HACD nanofibers (MitP-MNP, 10 mg/liter and HACD, 10 mg/liter) for an additional 24 hours. The cells were washed twice with PBS and examined by flow cytometry (FACSCalibur, BD Biosciences). Cells displaying strong FITC fluorescence were deemed to be bound to the MitP-MNP $\subset$ HACD nanofibers.

### Statistical analysis

Three replicates of each experiment were performed, and values reported herein are means  $\pm$  SD. Differences between groups were compared by a one-way analysis of variance (ANOVA) test ( $P < 0.05$ ). All statistical tests were performed using SPSS software package (version 20, IBM).

### SUPPLEMENTARY MATERIALS

Supplementary material for this article is available at <http://advances.sciencemag.org/cgi/content/full/4/9/eaat2297/DC1>

Table S1. Angles between the magnetic field line and the growth direction of supramolecular nanofibers and the growth rate of the MitP-MNP $\subset$ HACD assembly under different magnetic fields.

Fig. S1. Synthetic route of MitP-MNP.

Fig. S2. Characterization of the synthesized MNP, MitP, and MitP-MNP.

Fig. S3. Effect of HA, 1-adamantanecarboxylic acid, and arylazopyrazole on assembly of the nanofibers.

Fig. S4. Effect of ADA and artificial magnetic field on aggregation of mitochondria along with the direction of external magnetic field.

Fig. S5. Amplified confocal microscopy images of the A549 cells treated by MitP-MNP or MitP-MNP $\subset$ HACD.

Fig. S6. Localization of ABP-MNP as negative control.

Fig. S7. Effect of MitP-MNP, MitP-MNP $\subset$ HACD, and HACD on cell viability and cell death.

Fig. S8. Confocal microscopy images of MitP-MNP $\subset$ HACD in the Matrigel invasion model.

Fig. S9. Binding activity of MitP-MNP $\subset$ HACD with the tumor cells (A549-RFP) and the normal cells (293T) and the impact of the nanofibers on the RES organs.

Movie S1. Confocal microscopic observation of MitP-MNP and HACD aggregate in the geomagnetism field.

Movie S2. Confocal microscopic observation of MitP-MNP and HACD aggregate in the geomagnetism field with different sample locations.  
 Movie S3. Microscopic observation of MitP-MNP and HACD aggregate upon deviation from Earth's magnetic field line.  
 Movie S4. Microscopic observation of MitP-MNP and HACD aggregate with a canceling system for artificial magnetism fields.  
 Movie S5. Microscopic observation of MitP-MNP and HACD aggregate in a metal-caged room.  
 Movie S6. Microscopic observation of MitP-MNP and HACD aggregate in an artificial magnetic field (0.308 mT).  
 Movie S7. Microscopic observation of MitP-MNP and HACD aggregate in an artificial magnetic field (2.968 mT).

## REFERENCES AND NOTES

- P. S. Steeg, Tumor metastasis: Mechanistic insights and clinical challenges. *Nat. Med.* **12**, 895–904 (2006).
- S. Valastyan, R. A. Weinberg, Tumor metastasis: Molecular insights and evolving paradigms. *Cell* **147**, 275–292 (2011).
- D. F. Quail, J. A. Joyce, Microenvironmental regulation of tumor progression and metastasis. *Nat. Med.* **19**, 1423–1437 (2013).
- L. Ma, F. Reinhardt, E. Pan, J. Soutschek, B. Bhat, E. G. Marcussen, J. Teruya-Feldstein, G. W. Bell, R. A. Weinberg, Therapeutic silencing of miR-10b inhibits metastasis in a mouse mammary tumor model. *Nat. Biotechnol.* **28**, 341–347 (2010).
- J. M. L. Ebos, R. S. Kerbel, Antiangiogenic therapy: Impact on invasion, disease progression, and metastasis. *Nat. Rev. Clin. Oncol.* **8**, 210–221 (2011).
- H. Yang, B. Yuan, X. Zhang, O. A. Scherman, Supramolecular chemistry at interfaces: Host-guest interactions for fabricating multifunctional biointerfaces. *Acc. Chem. Res.* **47**, 2106–2115 (2014).
- H.-L. Sun, Y. Chen, X. Han, Y. Liu, Tunable supramolecular assembly and photoswitchable conversion of cyclodextrin/diphenylalanine-based 1D and 2D nanostructures. *Angew. Chem. Int. Ed. Engl.* **56**, 7062–7065 (2017).
- P. Tanner, P. Baumann, R. Enea, O. Onaca, C. Palivan, W. Meier, Polymeric vesicles: From drug carriers to nanoreactors and artificial organelles. *Acc. Chem. Res.* **44**, 1039–1049 (2011).
- M. J. Webber, E. A. Appel, E. W. Meijer, R. Langer, Supramolecular biomaterials. *Nat. Mater.* **15**, 13–26 (2016).
- X. Du, J. Zhou, J. Shi, B. Xu, Supramolecular hydrogelators and hydrogels: From soft matter to molecular biomaterials. *Chem. Rev.* **115**, 13165–13307 (2015).
- X. Ma, Y. Zhao, Biomedical applications of supramolecular systems based on host-guest interactions. *Chem. Rev.* **115**, 7794–7839 (2015).
- M. Karimi, A. Ghasemi, P. S. Zangabad, R. Rahighi, S. M. M. Basri, H. Mirshekari, M. Amiri, Z. S. Pishabad, A. Aslani, M. Bozorgomid, D. Ghosh, A. Beyzavi, A. Vaseghi, A. R. Aref, L. Haghani, S. Bahrami, M. R. Hamblin, Smart micro/nanoparticles in stimulus-responsive drug/gene delivery systems. *Chem. Soc. Rev.* **45**, 1457–1501 (2016).
- K. Ulbrich, K. Holá, V. Subr, A. Bakandritsos, J. Tuček, R. Zbořil, Targeted drug delivery with polymers and magnetic nanoparticles: Covalent and noncovalent approaches, release control, and clinical studies. *Chem. Rev.* **116**, 5338–5431 (2016).
- T. Ahn, J. H. Kim, H.-M. Yang, J. W. Lee, J.-D. Kim, Formation pathways of magnetite nanoparticles by coprecipitation method. *J. Phys. Chem. C* **116**, 6069–6076 (2012).
- L. Ji, Z. Tan, T. R. Kuykendall, S. Aloni, S. Xun, E. Lin, V. Battaglia, Y. Zhang, Fe<sub>3</sub>O<sub>4</sub> nanoparticle-integrated graphene sheets for high-performance half and full lithium ion cells. *Phys. Chem. Chem. Phys.* **13**, 7170–7177 (2011).
- K. L. Horton, K. M. Stewart, S. B. Fonseca, Q. Guo, S. O. Kelley, Mitochondria-penetrating peptides. *Chem. Biol.* **15**, 375–382 (2008).
- Y. Yang, Y.-M. Zhang, Y. Chen, J.-T. Chen, Y. Liu, Targeted polysaccharide nanoparticle for adamplatin prodrug delivery. *J. Med. Chem.* **56**, 9725–9736 (2013).
- L. Stricker, E.-C. Fritz, M. Peterlechner, N. L. Doltsinis, B. J. Ravoo, Arylazopyrazoles as light-responsive molecular switches in cyclodextrin-based supramolecular systems. *J. Am. Chem. Soc.* **138**, 4547–4554 (2016).
- M. T. Jeena, L. Palanikumar, E. M. Go, I. Kim, M. G. Kang, S. Lee, S. Park, H. Choi, C. Kim, S.-M. Jin, S. C. Bae, H. W. Rhee, E. Lee, S. K. Kwak, J.-H. Ryu, Mitochondria localization induced self-assembly of peptide amphiphiles for cellular dysfunction. *Nat. Commun.* **8**, 26 (2017).
- C. Higashida, T. Kiuchi, Y. Akiba, H. Mizuno, M. Maruoka, S. Narumiya, K. Mizuno, N. Watanabe, F- and G-actin homeostasis regulates mechanosensitive actin nucleation by formins. *Nat. Cell Biol.* **15**, 395–405 (2013).
- L. Y. Li, X. Luo, X. Wang, Endonuclease G is an apoptotic DNase when released from mitochondria. *Nature* **412**, 95–99 (2001).
- I. C. Lopez-Mejia, L. Fajas, Cell cycle regulation of mitochondrial function. *Curr. Opin. Cell Biol.* **33**, 19–25 (2015).
- H. He, J. Wang, H. Wang, N. Zhou, D. R. Green, B. Xu, Enzymatic cleavage of branched peptides for targeting mitochondria. *J. Am. Chem. Soc.* **140**, 1215–1218 (2018).
- Z. Feng, H. Wang, X. Chen, B. Xu, Self-assembling ability determines the activity of enzyme-instructed self-assembly for inhibiting cancer cells. *J. Am. Chem. Soc.* **139**, 15377–15384 (2017).
- M.-Y. Lee, S.-J. Park, K. Park, K. S. Kim, H. Lee, S. K. Hahn, Target-specific gene silencing of layer-by-layer assembled gold-cysteamine/siRNA/PEI/HA nanocomplex. *ACS Nano* **5**, 6138–6147 (2011).
- K. Y. Choi, H. Y. Yoon, J.-H. Kim, S. M. Bae, R.-W. Park, Y. M. Kang, I.-S. Kim, I. C. Kwon, K. Choi, S. Y. Jeong, K. Kim, J. H. Park, Smart nanocarrier based on pegylated hyaluronic acid for cancer therapy. *ACS Nano* **5**, 8591–8599 (2011).

### Acknowledgments

**Funding:** This work was funded by the National Natural Science Foundation of China (grant nos. 21432004, 21472100, 21772099, and 91527301). **Author contributions:** Y.L., Q.Y., and Y.-M.Z. conceived and designed the experiments. Q.Y., Y.-H.L., and X.X. synthesized and performed the chemical characterization and biological experiments. Y.-M.Z. and Q.Y. wrote the main manuscript. Y.L. supervised the work and edited the manuscript. All authors analyzed and discussed the results and reviewed the manuscript. **Competing interests:** The authors declare that they have no competing interests. **Data and materials availability:** All data needed to evaluate the conclusions in the paper are present in the paper and/or the Supplementary Materials. Additional data related to this paper may be requested from the authors.

Submitted 6 February 2018  
 Accepted 30 July 2018  
 Published 19 September 2018  
 10.1126/sciadv.aat2297

**Citation:** Qu Yu, Y.-M. Zhang, Y.-H. Liu, X. Xu, Y. Liu, Magnetism and photo dual-controlled supramolecular assembly for suppression of tumor invasion and metastasis. *Sci. Adv.* **4**, eaat2297 (2018).

## Magnetism and photo dual-controlled supramolecular assembly for suppression of tumor invasion and metastasis

Qilin Yu, Ying-Ming Zhang, Yao-Hua Liu, Xun Xu and Yu Liu

*Sci Adv* 4 (9), eaat2297.  
DOI: 10.1126/sciadv.aat2297

ARTICLE TOOLS	<a href="http://advances.sciencemag.org/content/4/9/eaat2297">http://advances.sciencemag.org/content/4/9/eaat2297</a>
SUPPLEMENTARY MATERIALS	<a href="http://advances.sciencemag.org/content/suppl/2018/09/17/4.9.eaat2297.DC1">http://advances.sciencemag.org/content/suppl/2018/09/17/4.9.eaat2297.DC1</a>
REFERENCES	This article cites 26 articles, 0 of which you can access for free <a href="http://advances.sciencemag.org/content/4/9/eaat2297#BIBL">http://advances.sciencemag.org/content/4/9/eaat2297#BIBL</a>
PERMISSIONS	<a href="http://www.sciencemag.org/help/reprints-and-permissions">http://www.sciencemag.org/help/reprints-and-permissions</a>

Use of this article is subject to the [Terms of Service](#)

---

*Science Advances* (ISSN 2375-2548) is published by the American Association for the Advancement of Science, 1200 New York Avenue NW, Washington, DC 20005. 2017 © The Authors, some rights reserved; exclusive licensee American Association for the Advancement of Science. No claim to original U.S. Government Works. The title *Science Advances* is a registered trademark of AAAS.